SUPPORTING INFORMATION

Nanoplatelet Cryoaerogels for Potential Application in Photoelectrochemical Sensing

Anja Schlosser,[ab] *Lea C. Meyer,*[ab] *Franziska Lübkemann,*[ab] *Jan F. Miethe,*[ab] *and Nadja C. Bigall*[ab*]

[a] Institute of Physical Chemistry and Electrochemistry, Leibniz Universität Hannover, Callinstr. 3a, D-30167 Hannover, Germany

[b] Laboratory of Nano and Quantum Engineering (LNQE), Leibniz Universität Hannover, Schneiderberg 39, 30167 Hannover, Germany

* nadja.bigall@pci.uni-hannover.de

1 Platelet characterisation

1.1 As-synthesised CdSe NPLs.

Rectangular CdSe NPLs with a thickness of 4 monolayers (MLs) were synthesised according to a previously published procedure.[1] TEM images of the as-synthesised NPLs (Figure S1) show, that NPLs with a mean size of 22.8 nm ± 2.9 nm x 7.1 nm ± 1.4 nm were obtained. It is moreover visible, that the corners of the platelets are slightly rounded. The desired platelet thickness was confirmed by UV/vis and emission spectroscopy (Figure S3).

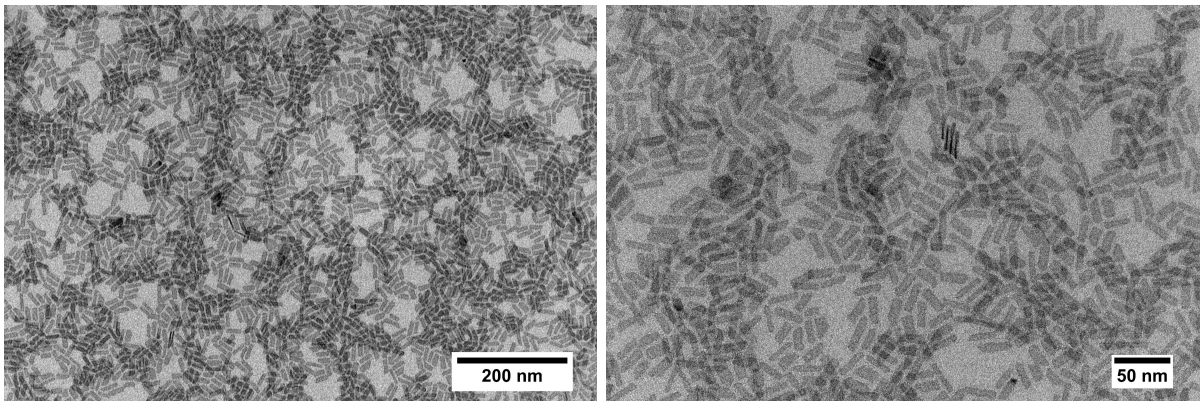

Figure S1. Additional TEM images of the as-synthesised CdSe NPLs in hexane in low magnification (left) and higher magnification (right).

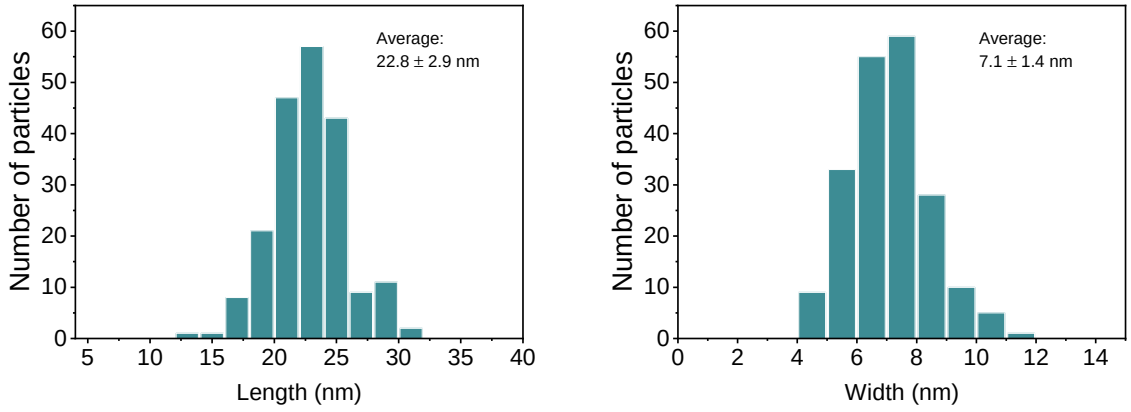

Figure S2. Particle size distribution of as-synthesised CdSe NPLs (n = 200). Left: Length of the NPLs. Right: Width of the NPLs.

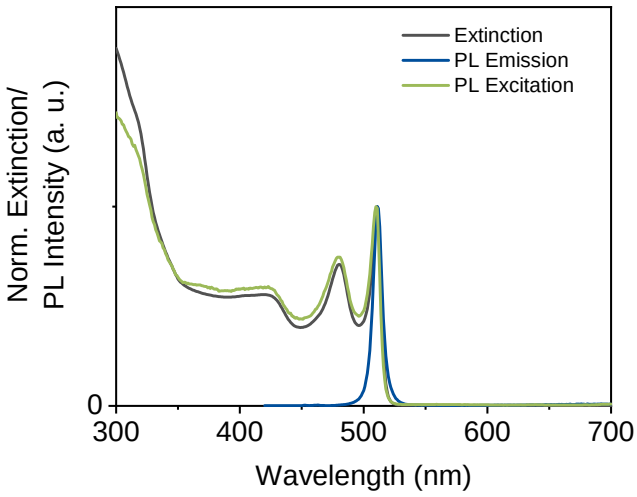

Figure S3. Optical characterisation of as-synthesised CdSe NPLs. The absorbance of the NPLs is shown in grey. The characteristic absorption features of 4 ML NPLs, corresponding to the light hole-electron(lh-e) and the heavy hole-electron (hh-e) transition, are located at 480 nm and 510 nm, respectively. The PL emission maximum is located at 511 nm (blue line) with a FWHM of 8 nm. The PL excitation is shown in green.

1.2 Phase-transferred CdSe NPLs.

The NPLs were transferred to aqueous solution by ligand exchange with 11-mercaptoundecanoic acid following a literature procedure with slight modifications.[2] Although the optical features of the NPLs appear to be weakened and strongly red-shifted after the phase transfer (Figure 2), the TEM images reveal, that the platelet shape is retained (Figure S4).

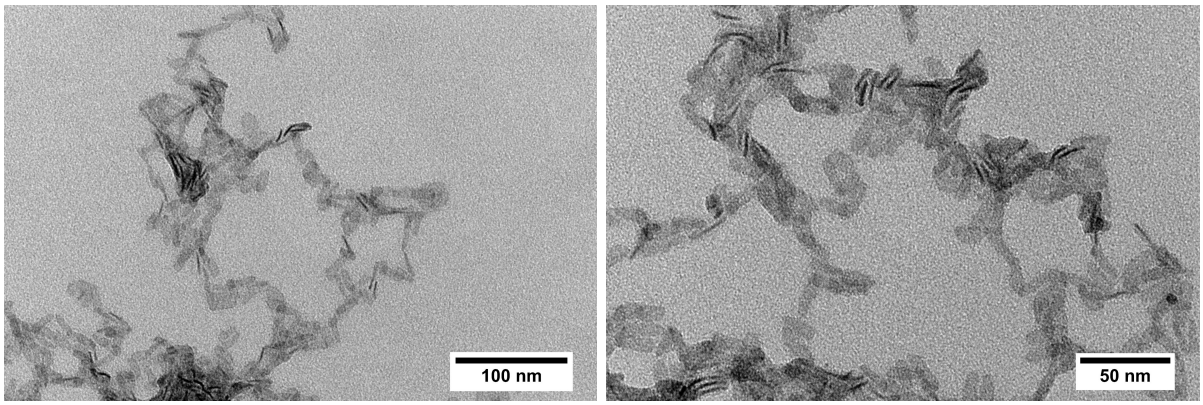

Figure S4. TEM images of the phase-transferred CdSe NPLs in low magnification (left) and higher magnification (right).

However, the fluorescence of the NPLs was observed to be completely quenched during the phase transfer. After the successful phase-transfer the NPLs were re-dispersed in differently concentrated KOH solutions and water.

It needs to be noted, that also other ligands (3-mercatopropyl acid (MPA) and 2-(dimethylamino)ethanethiol hydrochloride (DMAET)) than MUA were employed for the phase transfer of the NPLs, but no cryaerogel formation was observed in these cases. This could be attributed to the ligand concentration being too high for a successful cryoaerogelation process. Whereas the

ligand concentration in these two solutions could not be further reduced without destabilising the NPLs, NPLs coated with MUA could be sufficiently purified by a washing step with acetone. This washing step is crucial for the fabrication of cryoaerogel films on glass electrodes, as the attachment of the non-washed particles on the electrode surface is too low to allow any further characterisation (Figure S23).

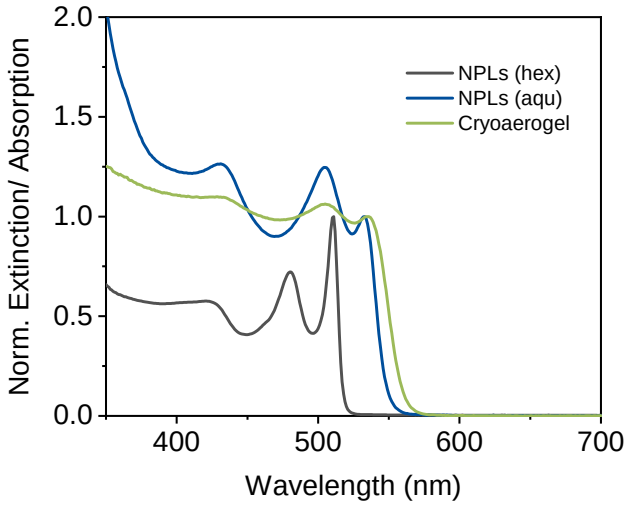

Figure S5. Normalised UV/vis extinction and absorption spectra of pristine CdSe NPLs (grey), phase-transferred CdSe NPLs (blue), and a CdSe NPL cryoaerogel (green).

2 Electrode characterisation

2.1 Photographs.

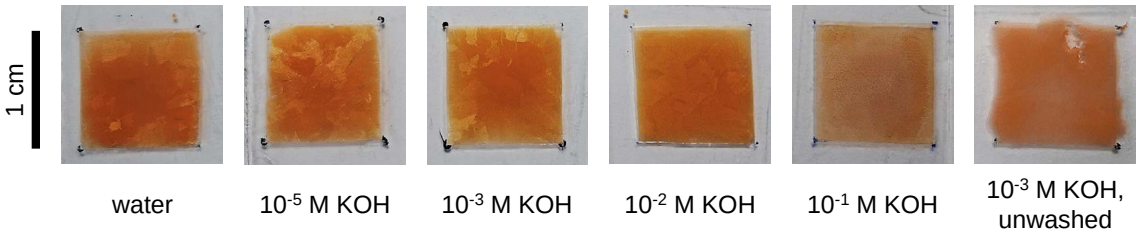

Figure S6. Photographs of the cryoaerogel coated parts of different photoelectrodes. In this series, the concentration of the KOH, which acts as a structure-defining agent, was varied. For the electrode preparation, 20 µL of the respective aqueous NPL solution was used.

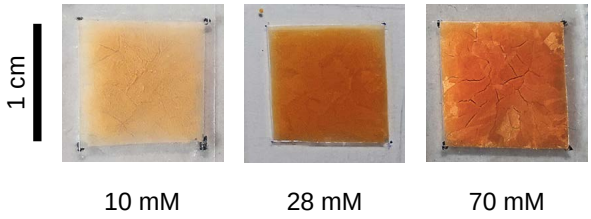

Figure S7. Photographs of the cryoaerogel coated parts of different photoelectrodes. In this series the concentration of the NPL solution was varied. For the electrode preparation, 20 µL of a NPL solution in $1 \cdot 10^{-2}$ M KOH was used.

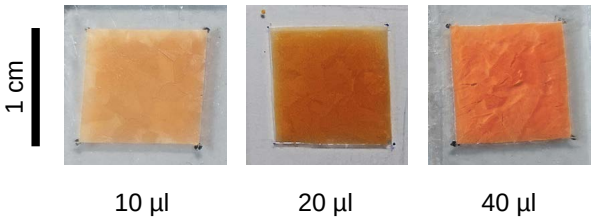

Figure S8. Photographs of the cryoaerogel coated parts of different photoelectrode. In this series the amount of the applied NPL solution was varied. For the electrode preparation, a 28 mM NPL solution in $1 \cdot 10^{-2}$ M KOH was used.

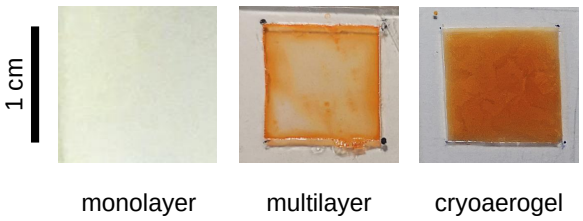

Figure S9. Photographs of a (sub-)monolayer, a multilayer, and a cryoaerogel photoelectrodes. For the preparation of the multilayer and the cryoaerogel electrode, 20 µL of a 28 mM NPL solution in $1 \cdot 10^{-2}$ M KOH were used.

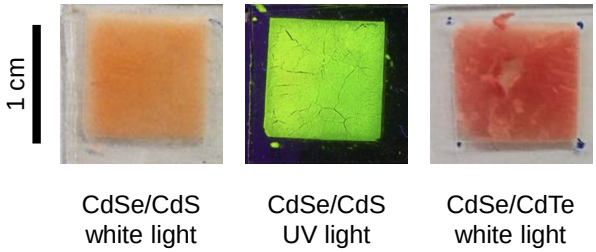

Figure S10. Photographs of cryoaerogel coatings based on heterostructured NPLs. Left: CdSe/CdS core/crown cryoaerogel under white light illumination. Middle: CdSe/CdS core/crown cryoaerogel under UV light illumination. Right: CdSe/CdTe core/crown cryoaerogel under white light illumination. For the electrode preparation, 20 µL of a 28 mM NPL solution in $1 \cdot 10^{-2}$ M KOH were used.

2.2 X-ray diffraction results.

Figure S11 displays the X-ray diffractograms (XRDs) of the as-synthesised and the phase-transferred NPLs as well as the XRD of a cryoaerogel. CdSe NPLs were obtained in the cubic zinc blende structure. The XRD patterns reveal, that the crystal structure does not change, neither during the phase-transfer nor during the cryogelation. The (220)-reflection of the as-synthesised NPLs was observed to be slightly asymmetric. This can be explained by the fact, that the lattice is not ideally cubic and therefore a splitting into two overlaying reflections takes place.[3] The XRDs of the phase-transferred NPLs and the cryoaerogel do not show this asymmetry, but the (220)-reflections are slightly shifted towards higher angles. This was attributed to the extension of the thickness confinement due to the ligand exchange.[3] However, if the widths of the (220)-reflections are compared, a slight decrease was observed for the cryoaerogel (compared to the phase-transferred NPLs). In general, this would reveal a growth of the crystallites due to the cryoaerogelaton. However, the decrease in the width could also be attributed to the background introduced by the grease, which was used for the sample preparation. In addition, the reflection splitting complicates the interpretation of the reflection width in this case, so that a reduction of the reflection width is not necessarily caused by crystallite growth.

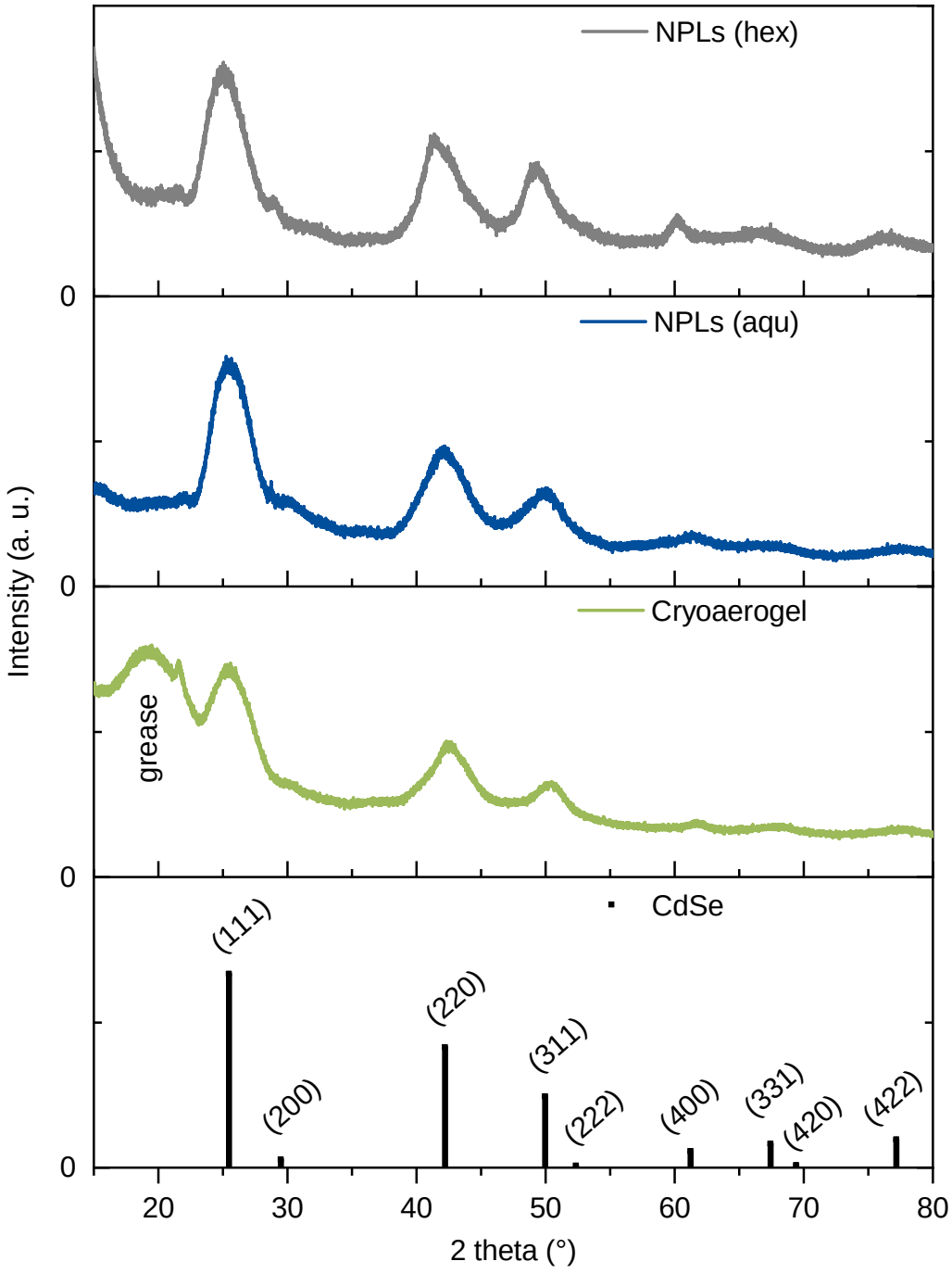

Figure S11. X-ray diffractograms of as-synthesised CdSe NPLs (grey), phase-transferred CdSe NPLs (blue), and a NPL-based cryoaerogel. Reflection positions and intensities of bulk zinc blende CdSe (PDF #03-065-2891) are shown in black.

2.3 Reproducibility and homogeneity of the cryoaerogel coating.

The homogeneity was evaluated on the millimetre-scale by UV/vis spectroscopy and on the micrometre-scale by SEM. At first, the UV/vis spectra of six identically fabricated photoelectrodes are shown in Figure S12. All electrodes were illuminated at the same position (middle of the cryoaerogel coating) during the measurement. The positions of the optical features of

the NPLs are similar for all electrodes, only their optical density varies slightly. The optical densities at the hh-e absorption range between 0.84 and 0.65. However, it was also observed, that the optical density of one cryoaerogel film is not completely homogeneous (Figure S13).

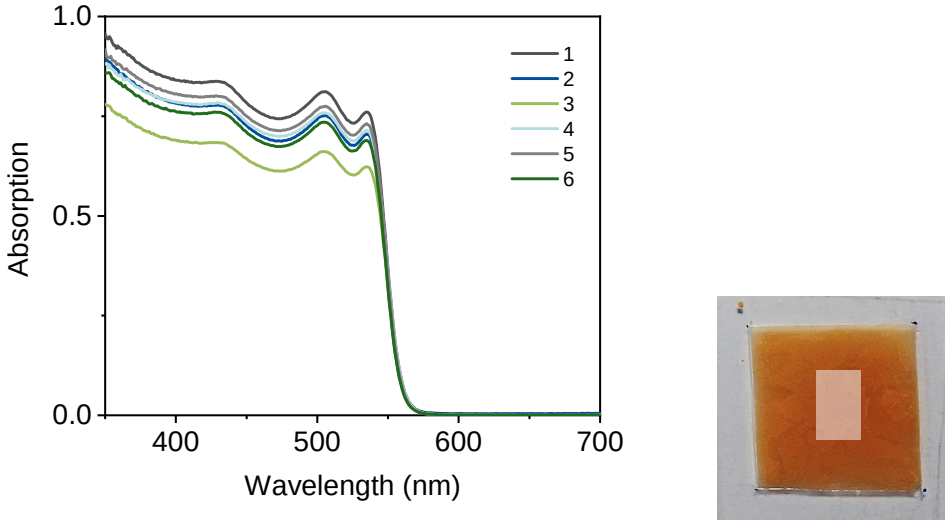

Figure S12. UV/vis absorption spectra of 6 identically fabricated photoelectrodes. Photoelectrodes were prepared with 20 µL of a NPL solution in $1 \cdot 10^{-2}$ M KOH. The right image shows the illumination spot during the measurement.

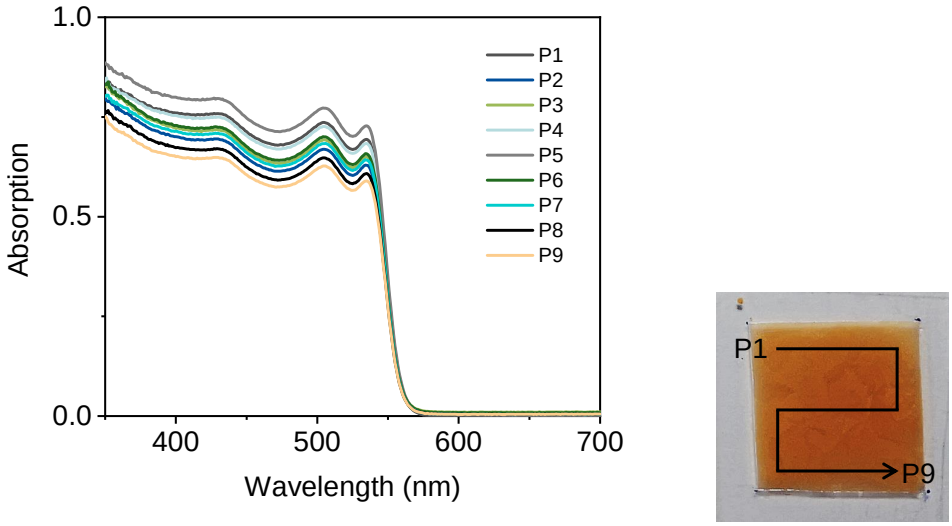

Figure S13. UV/vis absorption of one cryoaerogel coating measured at different positions of the coating. All in all, 9 positions were examined.

The results reveal that the coatings slightly differ from each other, but that these differences could be partially explained by variations in the coating density or thickness. The low magnification SEM images (Figure S14) support this thesis. As can be seen from Figure S14 B, the sheet density differs slightly for different electrode positions. Moreover, cracks are observed in the coatings, which were probably caused by the slight shrinkage of the cryoaerogels during the drying process. It can also be derived, that the sheets form domain-like structures. In the domains, they are aligned parallel to each other.

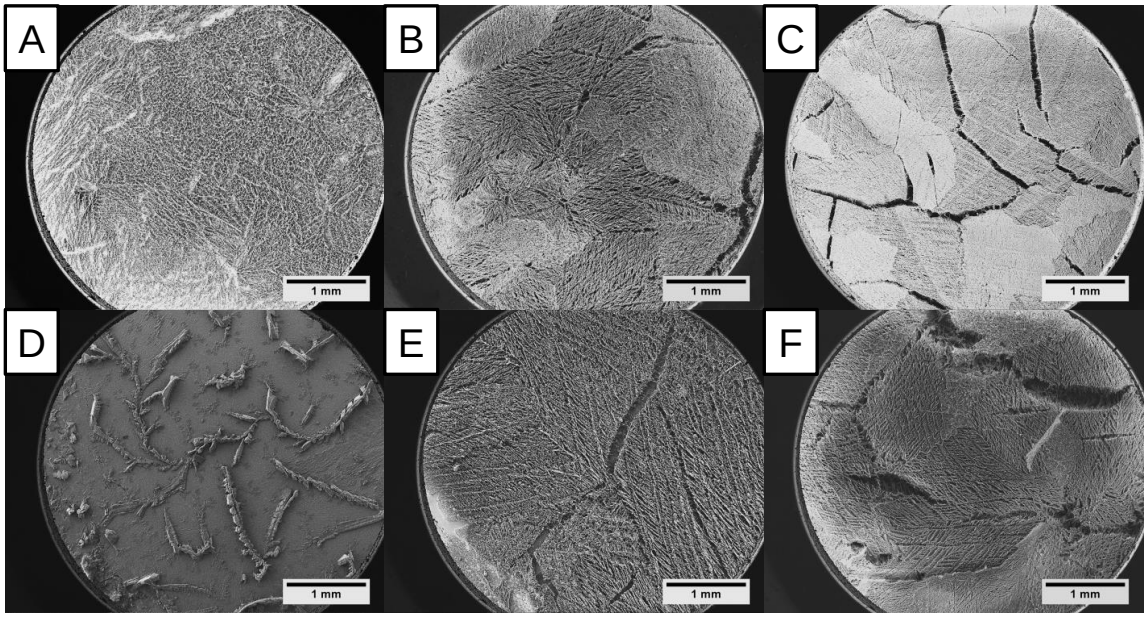

Figure S14. Low magnification SEM images of different cryaerogel films. Parameters are given as follows: volume of applied NPL solution, NPL concentration, KOH concentration. (A) 20 µL, 10 mM, $1 \cdot 10^{-2}$ M KOH, (B) 20 µL, 28 mM, $1 \cdot 10^{-2}$ M KOH, (C) 20 µL, 70 mM, $1 \cdot 10^{-2}$ M KOH, (D) 20 µL, 28 mM, $1 \cdot 10^{-1}$ M KOH, (E) 10 µL, 28 mM, $1 \cdot 10^{-2}$ M KOH, (F) 40 µL, 28 mM, $1 \cdot 10^{-2}$ M KOH.

The thickness of the coatings, in contrast, was observed to be nearly uniform. In Figure S15 SEM cross-section images of two different electrodes are shown. These reveal, that the coating of the electrode prepared with 40 µL is slightly thinner at the edges compared to the middle of the electrode. Most likely, this is caused by the fact, that the thickness of the adhesive tape and the applied solution did not match ideally.

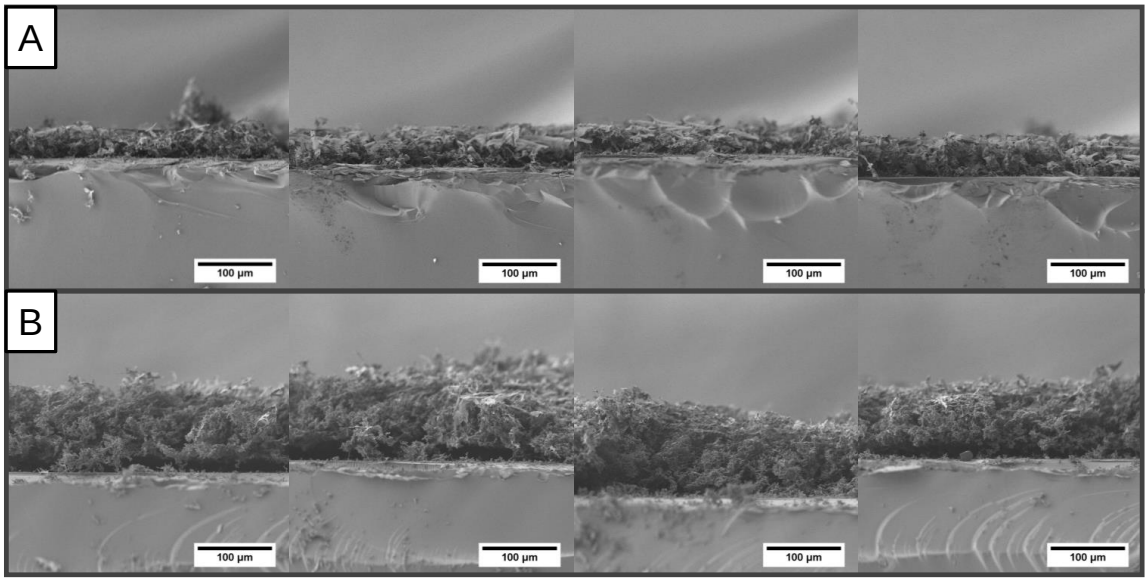

Figure S15. Cross-section SEM images of different cryaerogel films. (A) 10 µL solution volume, (B) 40 µL solution volume. For the preparation of both electrodes, a NPL solution with a concentration of 28 mM in $1 \cdot 10^{-2}$ M KOH was applied.

2.4 Comparison of (sub-)monolayer, multilayer, and cryoaerogel coated electrodes.

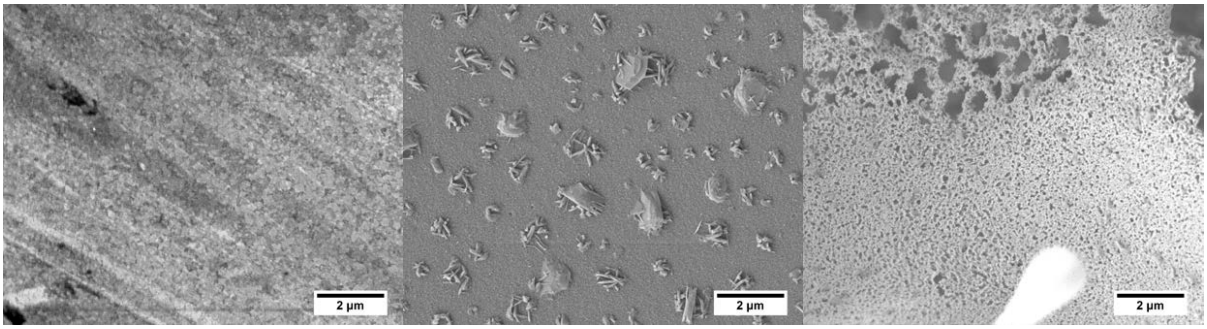

Figure S16. SEM micrographs of a NPL monolayer (left), a NPL multilayer (middle), and a NPL cryoaerogel (right). In case of the particle (sub-)monolayer, only the rough surface of the ITO coating is visible in this magnification. The SEM image of the multilayer reveals the formation needle-like KOH crystals on top of a dense layer of particles. The rough ITO surface is no longer visible. A porous structure is only formed, if the cryogelation method is used for electrode preparation. Note, that the right SEM image does not show the electrode surface but a part of the cryoaerogel coating.

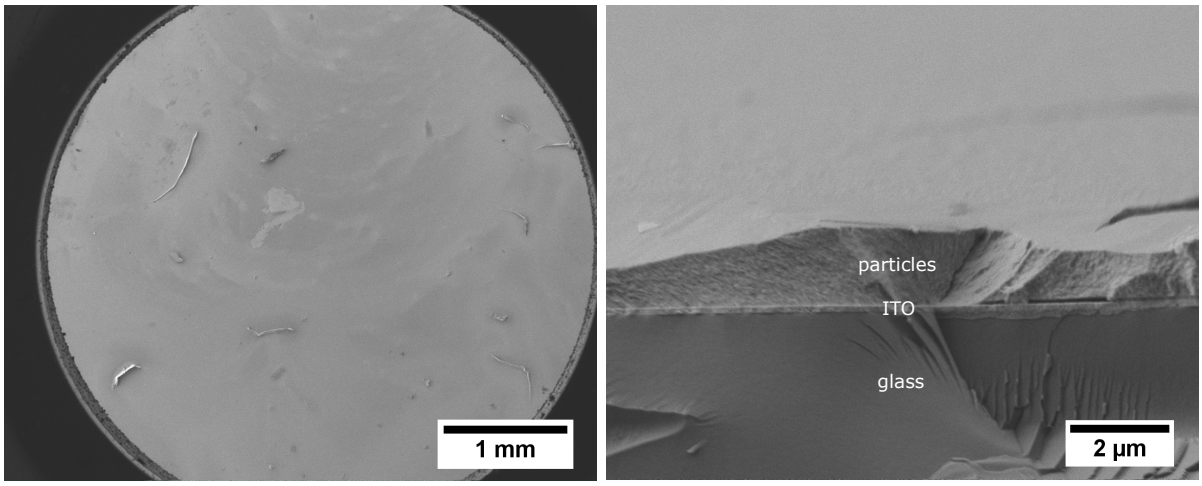

Figure S17. SEM micrographs of a NPL multilayer photoelectrode. Left: Micrograph of the surface in low magnification. Right: Micrograph of the cross-section. A dense layer with a thickness of around 2 µm on top of the ITO layer is visible.

2.5 Further characterisation results of the cryoaerogels.

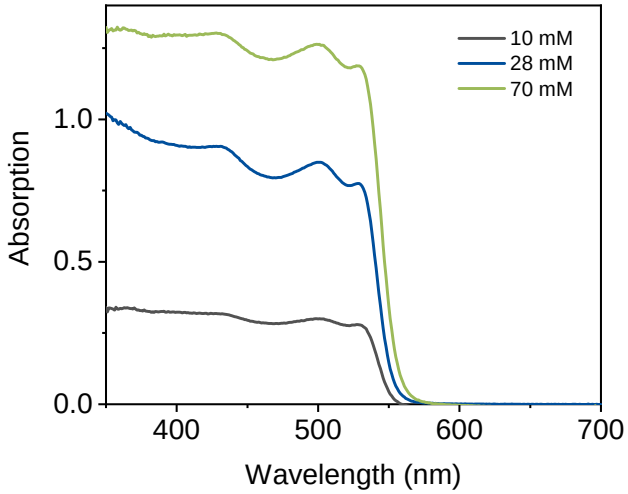

Figure S18. UV/vis absorption spectra coated with cryoaerogel films obtained from differently concentrated NPL solutions. Photoelectrodes were prepared with 20 µL of a NPL solution in $1 \cdot 10^{-2}$ M KOH.

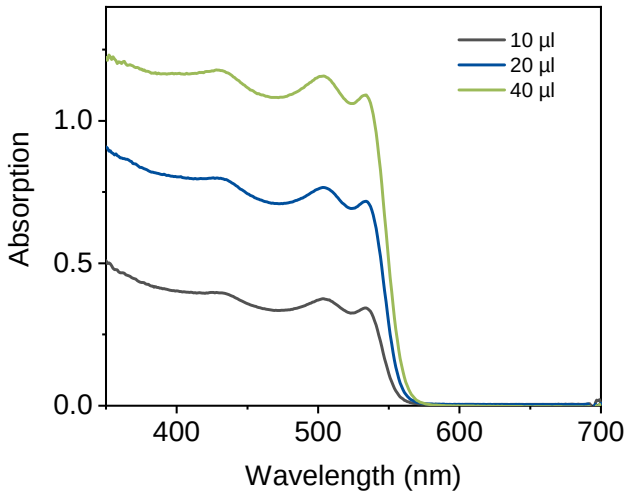

Figure S19. UV/vis absorption spectra of cryoaerogel films with different film thicknesses. The film thickness was varied by varying the NPL solution volume. Photoelectrodes were prepared from a 28 mM NPL solution in $1 \cdot 10^{-2}$ M KOH.

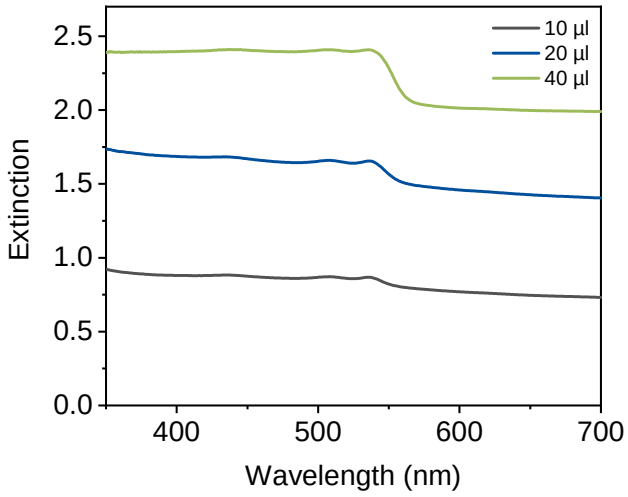

Figure S20. UV/vis extinction spectra of cryoaerogel films with different film thicknesses. The film thickness was varied by varying the NPL solution volume. Photoelectrodes were prepared from a 28 mM NPL solution in $1 \cdot 10^{-2}$ M KOH.

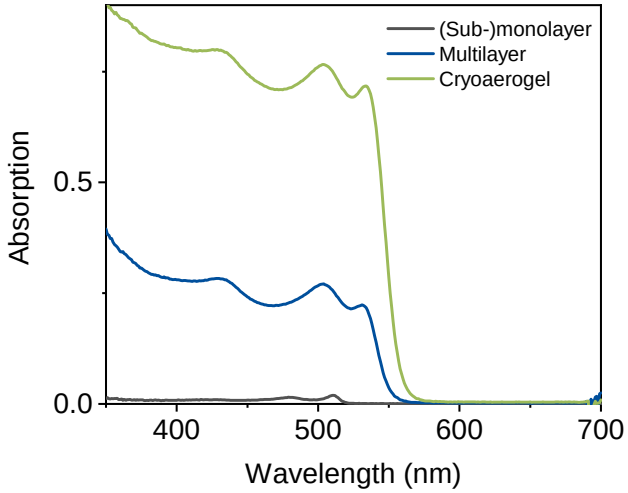

Figure S21. UV/vis absorption spectra of a (sub-)monolayer, a multilayer, and a cryoaerogel photoelectrode. For the preparation of the latter two electrodes, 20 µL of a 28 mM NPL solution in $1 \cdot 10^{-2}$ M KOH were used.

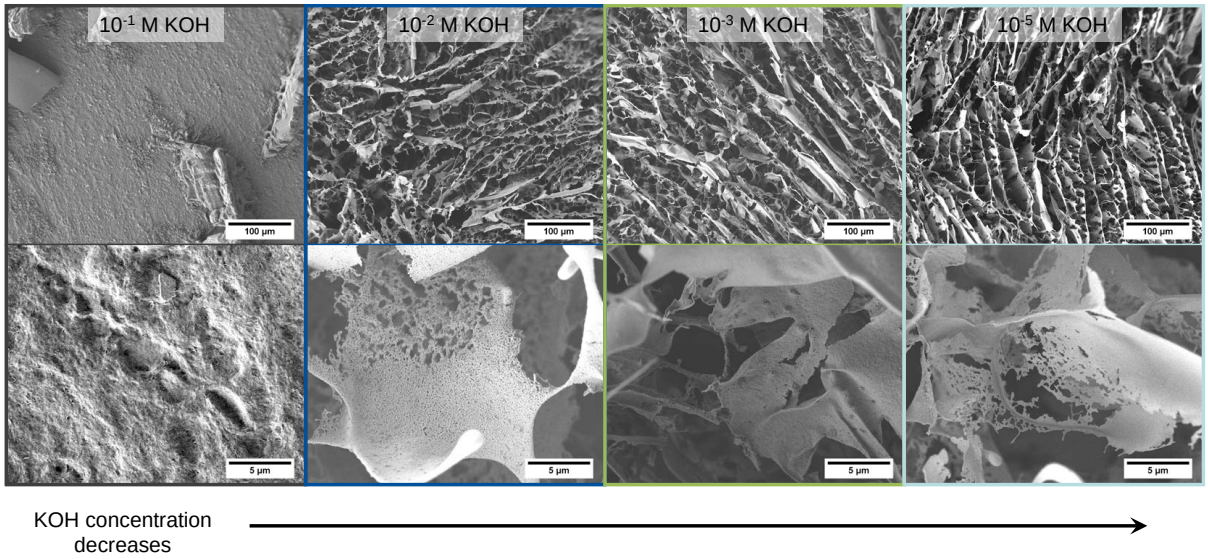

Figure S22. Influence of the KOH concentration on the morphology of the cryoaerogel coating. The concentration of KOH in the aqueous NPL solution decreases from left to right. Porous structures are only formed for KOH concentrations of less than or equal to $1 \cdot 10^{-2}$ M. The NPL concentration was kept constant at 28 mM, the solution volume was 20 µL.

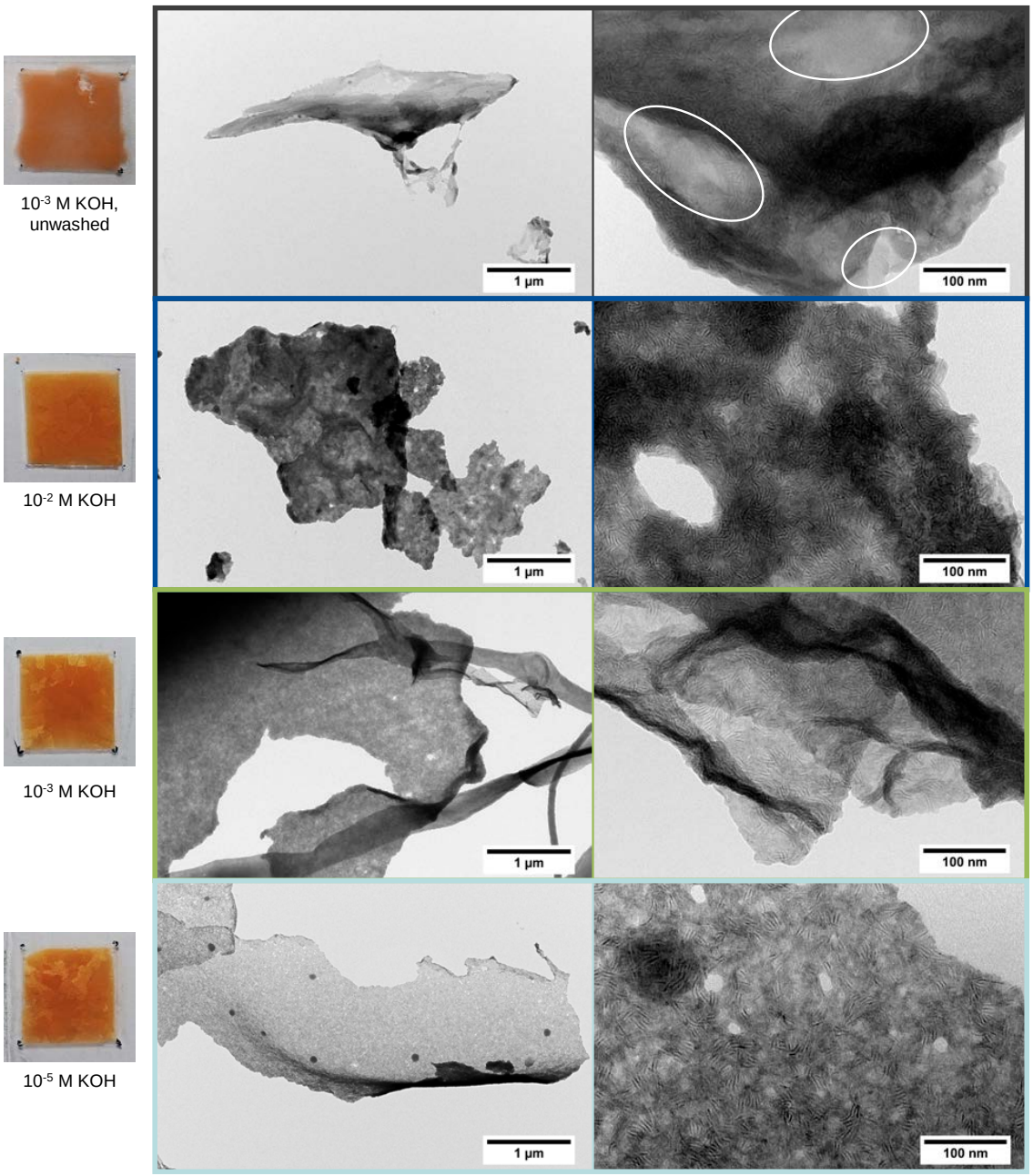

Figure S23. TEM micrographs of different cryoaerogel coatings. In all low magnification images, single sheets of the cryoaerogels are visible. The thickness of the sheets decreases with decreasing KOH concentration. If the NPLs are not washed after the phase transfer, the leaves do not only consist of NPLs but also of some material with a lower TEM contrast (white circles), probably organics (excess ligands). Cryoaerogels formed out of unwashed NPLs showed a much lower stability, especially in terms of substrate adhesion, and could therefore be characterised neither (photo-)electrochemically nor optically.

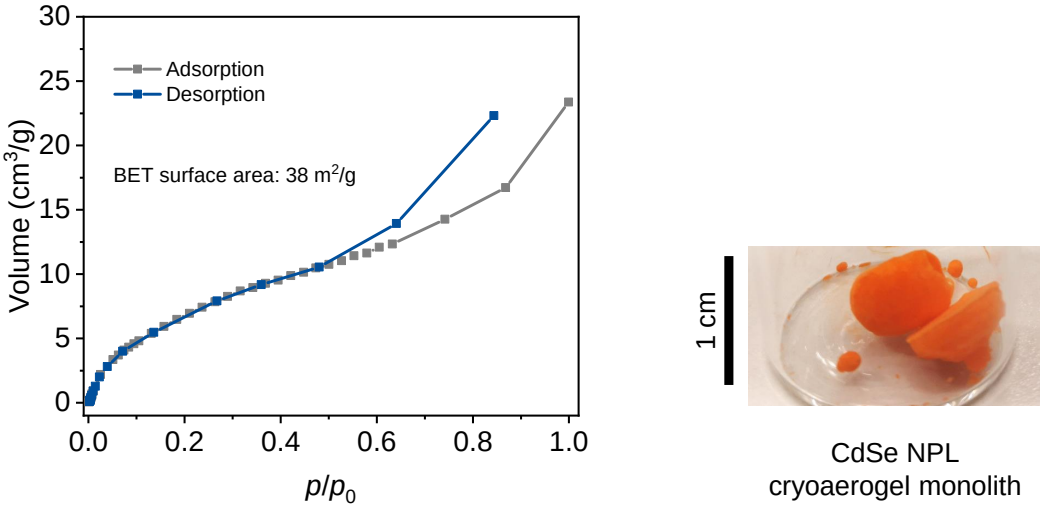

Figure S24. Left: Adsorption and desorption isotherm of a CdSe NPL cryoaerogel monolith obtained by Krypton physisorption measurements. A specific surface area of $38\,m^2\,g^{-1}$ was estimated by applying the Brunauer-Emmet-Teller (BET) equation. The determined surface area is comparable to the values previously reported for other semiconductor based cryoaerogels.[4] The recorded isotherm resembles the IUPAC Type II shape with a Type H3 hysteresis characteristic for macroporous adsorbents with a sheet-like structure.[5] This observation is in good agreement with the results of the SEM and TEM investigations of the material (Figure 2 C+D) which revealed the formation of CdSe NPL assemblies consisting of stacked non-porous sheets. Right: Photograph of the CdSe NPL monolith applied in the physisorption measurements.

3 Further photoelectrochemical data

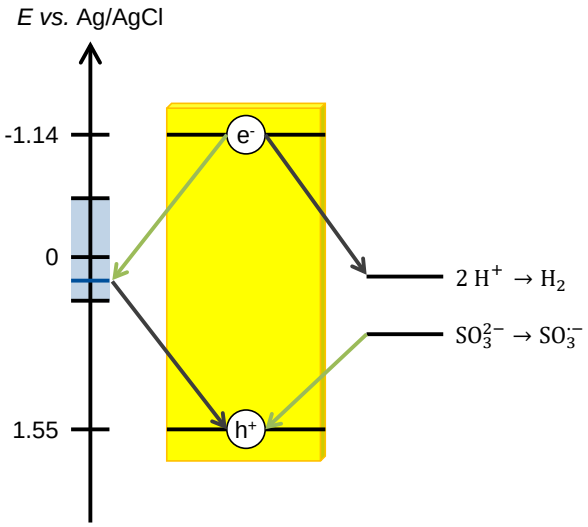

Figure S25. Possible reaction pathways in aqueous sodium sulfite solution under visible light illumination. All potentials are given for pH 9.5 and were derived from different literature sources.[6,7] The reduction of protons by excited electrons leads to negative photocurrents (grey arrows), whereas the oxidation of sulfite by photogenerated holes produces positive photocurrents (green arrows). The light blue bar represents the region in which the electrode potential was swept during the LSV measurements.

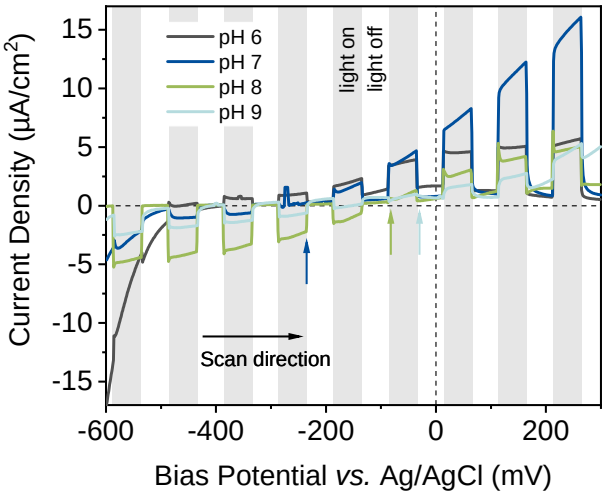

Figure S26. LSVs of a CdSe NPL cryoaerogel at different pH levels betwen 6 and 9. The arrows indicate the bias potentials, at which the sign of the photocurrent switches from negative to positive (photoelectrochemical photocurrent switching=PEPS). At pH 6, only positive photocurrents are generated. It needs to be noted, that the observed PEPS points can differ slightly for similarly prepared photoelectrodes, mainly due to slight variations in the ligand coverage of the particles. Cryoaerogel parameters: 20 µL NPL solution, 28 mM NPL concentration, $1 \cdot 10^{-2}$ M KOH concentration.

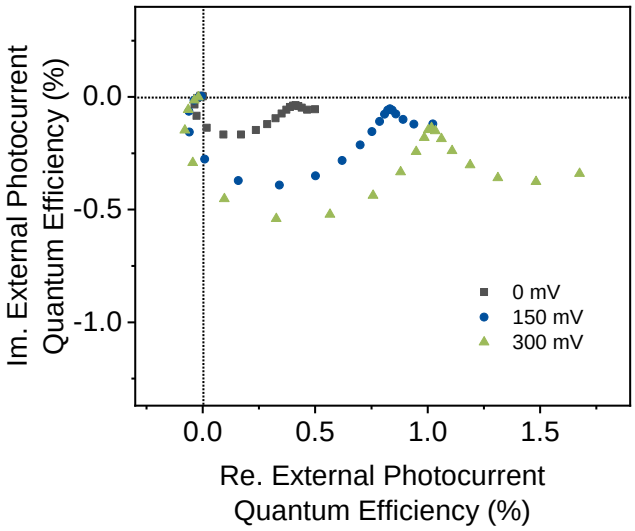

Figure S27. IMPS responses of the same cryoaerogel electrode measured at different bias potentials. Cryoaerogel parameters: 20 µL NPL solution, 28 mM NPL concentration, $1 \cdot 10^{-2}$ M KOH concentration.

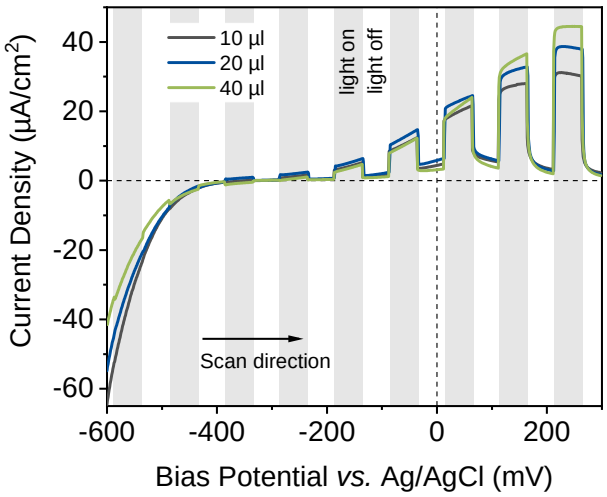

Figure S28. LSVs of CdSe NPL cryoaerogel coated photoelectrodes with different coating thicknesses. Cryoaerogel parameters: 10 µL, 20 µL, or 40 µL of NPL solution, 28 mM NPL concentration, $1 \cdot 10^{-2}$ M KOH concentration.

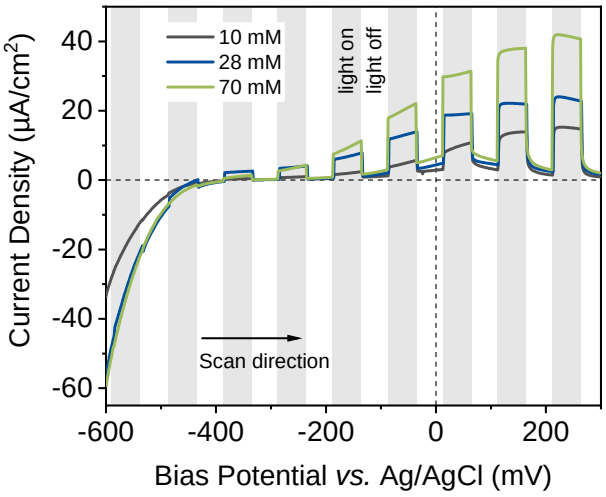

Figure S29. LSVs of CdSe NPL cryoaerogel coated photoelectrodes prepared from differently concentrated NPL solutions. Cryoaerogel parameters: 20 µL NPL solution, NPL concentration of 10 mM, 28 mM, or 70 mM, $1 \cdot 10^{-2}$ M KOH concentration. It needs to be noted, that all samples were prepared from the same NPL solution by dissolution with KOH. However, the used NPL solution is different to the solution applied for the preparation of the photoelectrodes characterised in Figure S28.

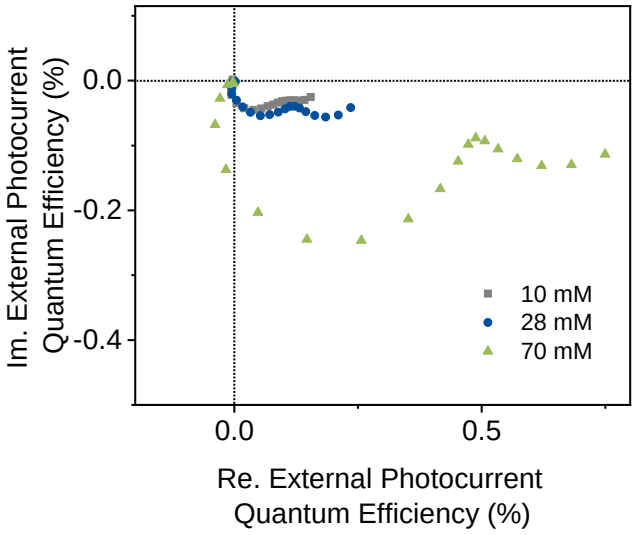

Figure S30. IMPS responses of CdSe NPL cryoaerogel coated photoelectrodes prepared from differently concentrated NPL solutions. Cryoaerogel parameters: 20 µL NPL solution, NPL concentration of 10 mM, 28 mM, or 70 mM, $1 \cdot 10^{-2}$ M KOH concentration.

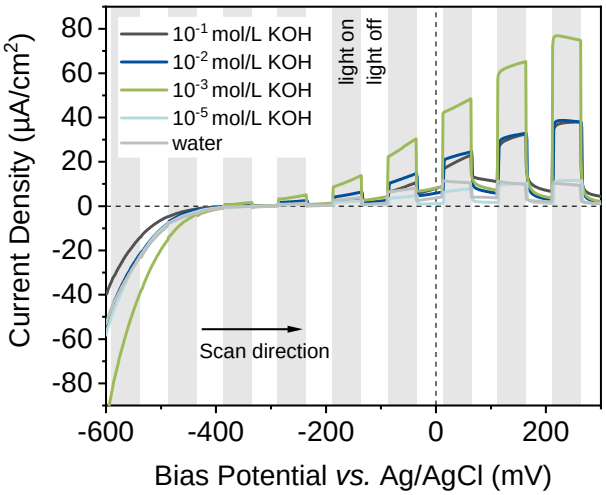

Figure S31. LSVs of CdSe NPL cryoaerogel coated photoelectrodes prepared from NPL solutions with different KOH concentrations. Cryoaerogel parameters: 20 µL NPL solution, 28 mM NPL concentration, KOH concentration of $1 \cdot 10^{-1}$ M $1 \cdot 10^{-2}$ M, $1 \cdot 10^{-3}$ M, $1 \cdot 10^{-5}$ M, or 0 M (water).

4 Additional data regarding photoelectrochemical sensing

The data points determined in the sensing experiments were fitted using the following function:

$$I_\mathrm{P} = I_0 + A_1 \cdot \left[1 - \mathrm{e}^{\left(\frac{-c_\mathrm{F}}{t_1}\right)}\right] + A_2 \cdot \left[1 - \mathrm{e}^{\left(\frac{-c_\mathrm{F}}{t_2}\right)}\right] \tag{1}$$

The following parameters were obtained for the multilayer and the cryoaerogel, respectively:

Multilayer:
$I_0 = 0.343$
$A_1 = 1.03$
$t_1 = 223.67$
$A_2 = 0.82$
$t_2 = 1233.41$
$R^2 = 0.9977$

Cryoaerogel:
$I_0 = 0.229$
$A_1 = 3.81$
$t_1 = 689.23$
$A_2 = 2.86$
$t_2 = 183.08$
$R^2 = 0.9988$

I_0 can be interpreted as the photocurrent at a ferricyanide concentration of $c_\mathrm{F} = 0\,\mu\mathrm{M}$. The two terms containing the exponential functions express the response of the photoelectrodes to changes in the ferricyanide concentration.

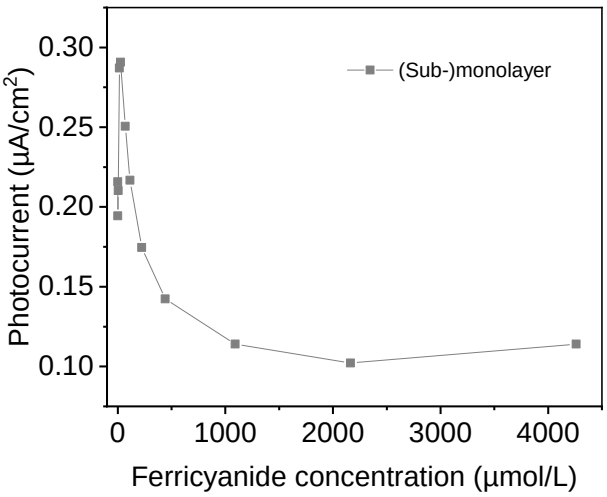

Figure S32. Photoresponse of a (sub-)monolayer photoelectrode to different ferricyanide concentrations. The line in between the data points was inserted to enhance the distinction of the data points especially in the low concentration range.

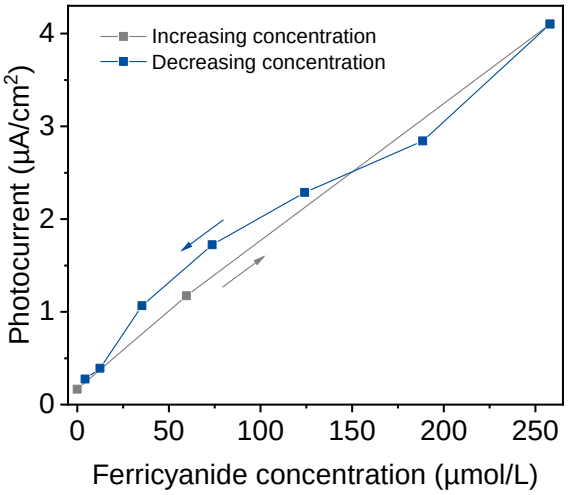

Figure S33. Photoresponse of a CdSe NPL photoelectrode to different ferricyanide concentrations.At first, the ferricyanide concentration was increased quickly to 260 µM. Then, the ferricyanide concentration was gradually decreased by removing 1/10 of the electrolyte volume from the measurement cell and refilling the cell wih fresh phosphate buffer. The line in between the data points was inserted to enhance the distinction between the two parts of the experiment.

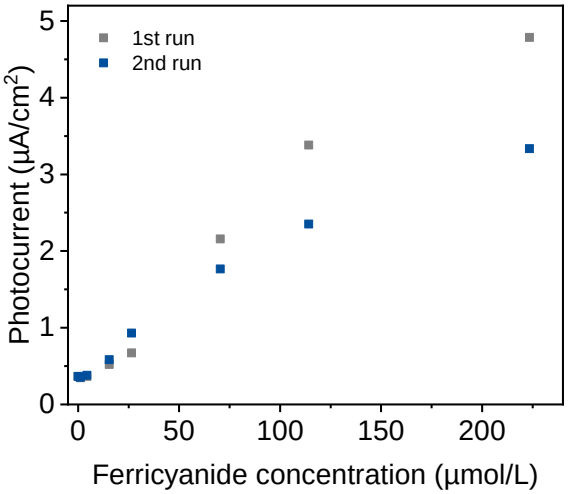

Figure S34. Photoresponse of a CdSe NPL photoelectrode to different ferricyanide concentrations. After an equilibration time of 1 h, the ferricyanide concentration in the phosphate buffer was increased gradually (grey squares, 1st run). After a concentration of 224 µmol L^{-1} was reached, the electrolyte solution in the measurement cell was removed and the measurement cell (containing the cryoaerogel working electrode) was rinsed several times with phosphate buffer. Subsequently, the ferricyanide concentration was increased to 224 µmol L^{-1} again (blue squares, 2nd run).
The sensitivity of the cryoaerogel electrode was observed to decrease slightly between the two runs. We attribute this to the fact, that the cryoaerogel structure is very sensitive to turbulences in the fully hydrated state so that some parts of the cryoaerogel may have desorbed from the electrode during the rinsing process.

5 Details on the photoelectrochemical setup

Electrochemical measurements were carried out using a ModuLab XM ECS potentiostat from Solartron, a Hameg HMF 2525 frequency generator from Rohde und Schwarz, and a 7270 general purpose DSP lock-in amplifier from Signal Recovery. A FDS100 Si photodiode purchased from ThorLabs was applied to measure the photon flux of the 468 nm LED (Figure S36). In order to avoid photocurrents which are too high to be processed by the lock-in amplifier, grey filters were inserted between the light source and the photodiode. The applied Ag/AgCl reference electrodes (3 M NaCl electrolyte) were purchased from BASi (type RE-5B). Every potential mentioned was measured in relation to this electrode type. As the counter electrode, a roughened platinum wire was applied. ITO glass was purchased from VisionTek Systems Ltd. The geometrical area of the working electrode in touch with the electrolyte is a circle with a diameter of 5 mm and an area of 0.2 cm^2.

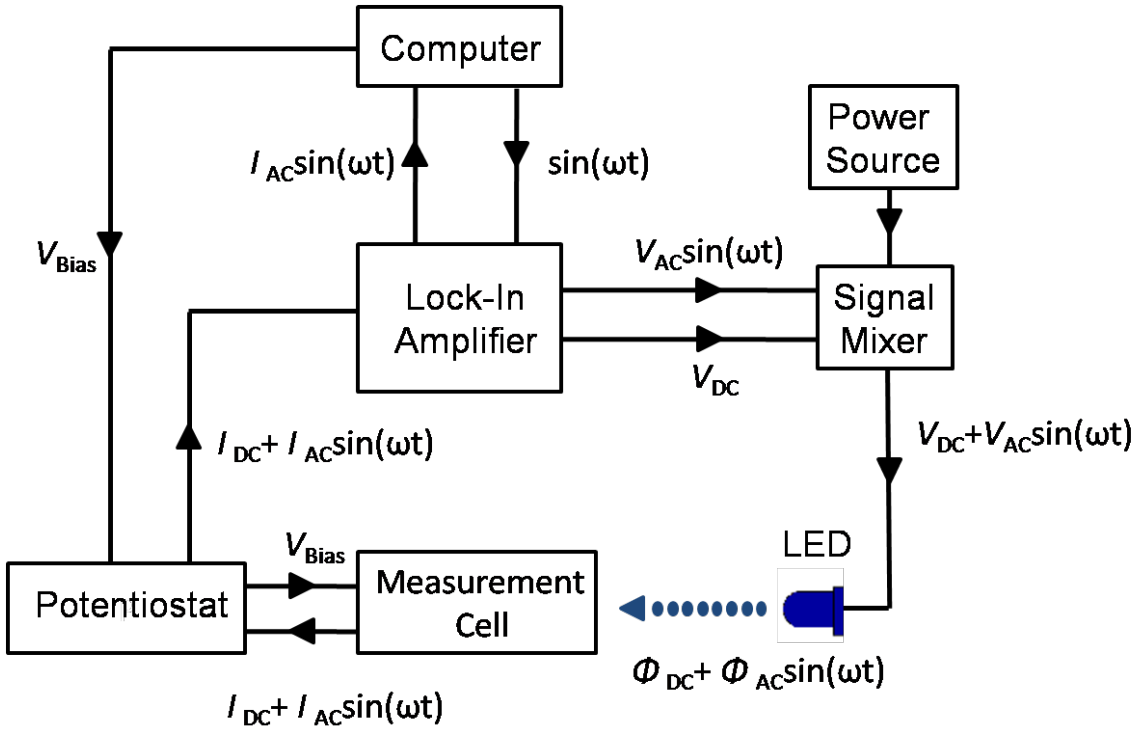

Figure S35. Scheme of the measurement setup for determination of intensity modulated photocurrent spectra.[8]

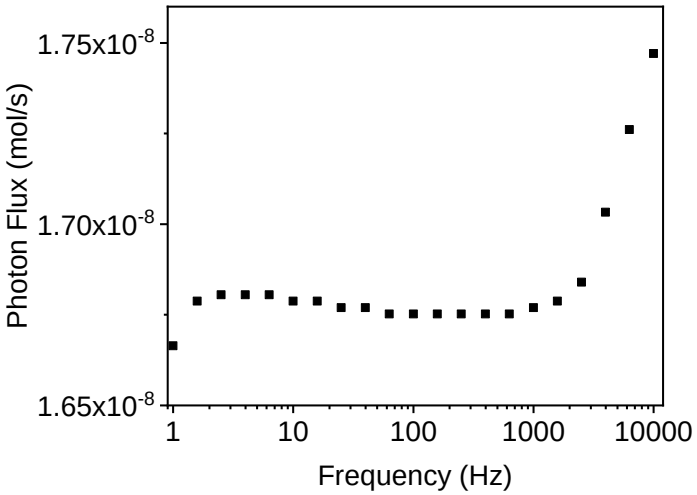

Figure S36. Frequency dependent light intensity of the 468 nm LED applied for the IMPS measurements.

References

[1] S. Pedetti, S. Ithurria, H. Heuclin, G. Patriarche and B. Dubertret, *Journal of the American Chemical Society*, 2014, **136**, 16430–16438.

[2] T. Kodanek, H. M. Banbela, S. Naskar, P. Adel, N. C. Bigall and D. Dorfs, *Nanoscale*, 2015, **7**, 19300–19309.

[3] A. Antanovich, A. W. Achtstein, A. Matsukovich, A. Prudnikau, P. Bhaskar, V. Gurin, M. Molinari and M. Artemyev, *Nanoscale*, 2017, **9**, 18042–18053.

[4] A. Freytag, C. Günnemann, S. Naskar, S. Hamid, F. Lübkemann, D. Bahnemann and N. C. Bigall, *ACS Applied Nano Materials*, 2018, **1**, 6123–6130.

[5] M. Thommes, K. Kaneko, A. V. Neimark, J. P. Olivier, F. Rodriguez-Reinoso, J. Rouquerol and K. S. Sing, *Pure and Applied Chemistry*, 2015, **87**, 1051–1069.

[6] D. Spittel, J. Poppe, C. Meerbach, C. Ziegler, S. G. Hickey and A. Eychmüller, *ACS Nano*, 2017, **11**, 12174–12184.

[7] T. N. Das, R. E. Huie and P. Neta, *The Journal of Physical Chemistry A*, 1999, **103**, 3581–3588.

[8] J. F. Miethe, F. Lübkemann, J. Poppe, F. Steinbach, D. Dorfs and N. C. Bigall, *ChemElectroChem*, 2018, **5**, 175–186.